# Water Oxidation at Hematite Photoelectrodes with an Iridium-Based Catalyst

Laura Badia-Bou,[†] Elena Mas-Marza,[‡] Pau Rodenas,[†] Eva M. Barea,[†] Francisco Fabregat-Santiago,[†] Sixto Gimenez,*,[†] Eduardo Peris,*,[‡] and Juan Bisquert*,[†]

[†]Photovoltaics and Optoelectronic Devices Group, Departament de Física, and [‡]Departament de Química Inorgànica & Orgànica, Universitat Jaume I, 12071 Castelló, Spain

S *Supporting Information*
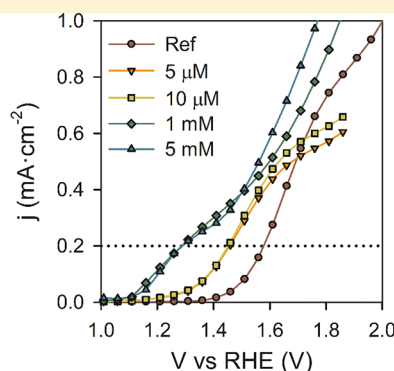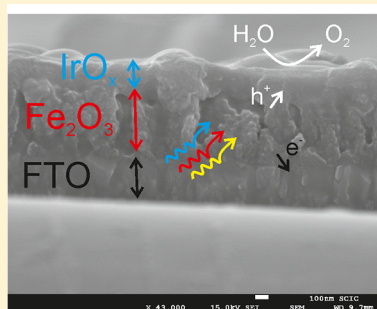
ABSTRACT: The iridium complex $[Cp*Ir(H_2O)_3](SO_4)$ was used as an organometallic source for the electrodeposition of iridium oxide onto Fe_2O_3. The new iridium-containing electrode allowed us to study the coupling between the photocatalytic properties of hematite and the electrocatalytic properties of the iridium-based material. A cathodic shift of the photocurrent for water oxidation upon electrodeposition of the iridium complex was observed, which increased with increasing surface concentration of IrO_x on Fe_2O_3. The shift for the highest surface concentration of iridium tested amounts to 300 mV at 200 $\mu A \cdot cm^{-2}$ current density. The catalytic mechanism of the IrO_x layer was unveiled by impedance spectroscopy measurements fitted to a physical model and can be explained on the basis of a highly capacitive layer, which enhances charge separation and stores photogenerated holes at Fe_2O_3, subsequently oxidizing water. These findings improve our understanding of the mechanism of water oxidation by heterogeneous Ir-based catalysts coupled to semiconductor electrodes.

INTRODUCTION

The efficient generation of hydrogen by photoelectrochemical water splitting with semiconductor materials has become one of the strategic scientific and technological key targets to face the energy problem in the forthcoming years.[1−4] Inspired by photosynthesis, this approach relies on the harvesting of solar energy and its storage in the form of chemical bonds to produce solar fuels, which can be used upon demand. To achieve this goal, a semiconductor material must satisfy certain stringent requirements including: (i) visible light absorption, (ii) appropriate positions of the conduction and valence band energy levels with respect to the relevant reaction potentials, (iii) efficient charge separation, (iv) good transport properties, (v) facile interfacial charge-transfer kinetics, and (vi) good stability in contact with aqueous solutions.[4] To date, no single material has fulfilled all the required conditions.

Hematite has shown extraordinary promising properties for solar water splitting due to its combination of abundance, visible light absorption (up to ~600 nm), stability in harsh conditions, and a valence band energy level sufficiently low to oxidize water.[5−7] These advantageous properties are balanced by its inherent low conductivity and a low energy level conduction band incapable of reducing H_2. The low conductivity of hematite together with its high light penetration depth can be overcome by nanostructuring strategies, which orthogonalize light absorption and carrier collection. As an example, one-dimensional core−shell structures like Fe_2O_3-coated Ti_2Si nanonets have shown improved performances.[8] On the other hand, raising the energy of electrons to facilitate the reduction of H_2 can be achieved by applying an external bias with a photovoltaic device or by integrating a small bandgap water-reduction system in a tandem configuration.[9]

Photoelectrochemical water oxidation at hematite electrodes also requires a large applied potential to produce a photocurrent. This large "overpotential" is believed to be caused by sluggish water oxidation kinetics at the hematite surface which competes with surface state recombination.[10,11] Consequently, different surface treatments (deposition of 13-group oxide overlayers,[12]

deposition of tiny layers of p-hematite[13]) and addition of catalysts (cobalt ions, the cobalt phosphate catalyst, "Co-Pi"[14−16], and IrO$_2$[17]) have been applied to minimize this problem.

Ir-based catalysts appear as ideal systems, located at the top end of the volcano plot for water oxidation catalysts by Trasatti.[4,18] Particularly, iridium oxides have the highest activities and turnover frequencies.[19] For the electrodeposition of iridium oxide films, several methods have been reported,[20−31] but recently Crabtree and Brudvig demonstrated that [Cp*Ir-(H$_2$O)$_3$](SO$_4$) (Scheme 1) is an excellent precursor for an

Scheme 1
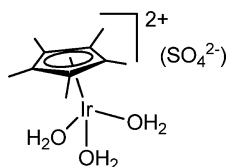
amorphous electrodeposited iridium catalyst.[32] In fact, they have highlighted the benefits of using iridium-based organometallic species as convenient sources of electrodeposited iridium oxides. They also have demonstrated that the cyclic voltammetric response of the electrodeposited material depends on the nature of the organometallic precursor used and does not match, in either case, with the responses given by iridium oxide anodes prepared from nonorganometallic precursors.[32]

Different pentamethylcyclopentadienyl (Cp*) derivatives have been demonstrated to be robust and highly active homogeneous catalysts for water oxidation when driven with cerium(IV)[33−36] and sodium periodate[37,38] as primary oxidants. Additionally, insight into the catalytic mechanisms (homogeneous vs heterogeneous catalysis) has become accessible by monitoring mass gain of the test electrodes by Electron Quartz Nanobalance (EQCN).[39,40]

In the present study, we have electrodeposited iridium oxide onto a Fe$_2$O$_3$ electrode using [Cp*Ir(H$_2$O)$_3$](SO$_4$) as the iridium source. Our initial aim is to study whether there should be any coupling between the photocatalytic properties of hematite with the electrocatalytic properties of the iridium electrodeposited material. Our final goal is the preparation of efficient photoanodes, to be integrated in water splitting photoelectrochemical solar cells. For this purpose, the electrodes must oxidize water with minimum overpotentials, affording large

oxygen evolution rates upon solar illumination. Complementarily, we want to evaluate the effect of the iridium catalyst electrodeposited onto hematite to improve our understanding about the mechanisms operating in the water oxidation catalysis.

■ EXPERIMENTAL METHOD

Hematite films were deposited onto FTO substrates (SnO$_2$:F, TEC 15) by Atmospheric Pressure Chemical Vapor Deposition (APCVD)[17,41] using 5×10^{-3} mol of Fe(CO)$_5$ as the iron precursor and TEOS (TetraEthylOrtoSilicate) as the Si doping agent (8 mol %). Prior to hematite deposition, the FTO substrates were exposed to ozone plasma during 30 min. Subsequently, the substrates were immersed into a 40 mM titanium chloride tetrahydrofuran complex solution during 30 min at 70 °C. Then, the substrates were heated at 400 °C in a hot plate, and APCVD took place. The reactive and carrier gases were directed vertically onto the heated substrate at 0.1 bar pressure.

The iridium oxide was electrodeposited onto Fe$_2$O$_3$ electrodes in a three-electrode cell from a solution of [Cp*Ir(H$_2$O)$_3$](SO$_4$) in 0.1 M KNO$_3$. Different surface concentrations of the catalyst on the surface of Fe$_2$O$_3$ were obtained, depending on the concentration of the organometallic iridium source in the solution (5 μM, 10 μM, 1 mM, and 5 mM). For electrodeposition, Fe$_2$O$_3$ was the working electrode; graphite was used as the counter electrode; and a Ag/AgCl electrode was used as reference. Deposition was carried out by applying 2 V vs Ag/AgCl during 1 h from the different [IrCp*]-containing solutions. After deposition the samples were rinsed in water and dried with air.

Cyclic voltammetry, steady state current density voltage ($j−V$), and Electrochemical Impedance Spectroscopy (EIS) were carried out using an FRA equipped PGSTAT-30 from Metrohm Autolab. A three-electrode configuration was used, where the Fe$_2$O$_3$/Ir photoelectrode was connected to the working electrode; a Pt wire was connected to the counterelectrode; and a saturated Ag/AgCl was used as the reference electrode. An aqueous solution buffered to pH 7 using a 0.1 M phosphate buffer (KH$_2$PO$_4$/K$_2$HPO$_4$) was used as electrolyte. Cyclic voltammetry measurements were carried out at 10 mV·s^{-1} unless otherwise stated. All the electrochemical measurements were referred to the reversible hydrogen electrode (RHE) by the equation $V_{RHE} = V_{Ag/AgCl} + 0.197 + pH(0.059)$. The electrodes were illuminated using a 450 W Xe lamp. The light intensity was adjusted with a thermopile to 100 mW/cm^2, with illumination
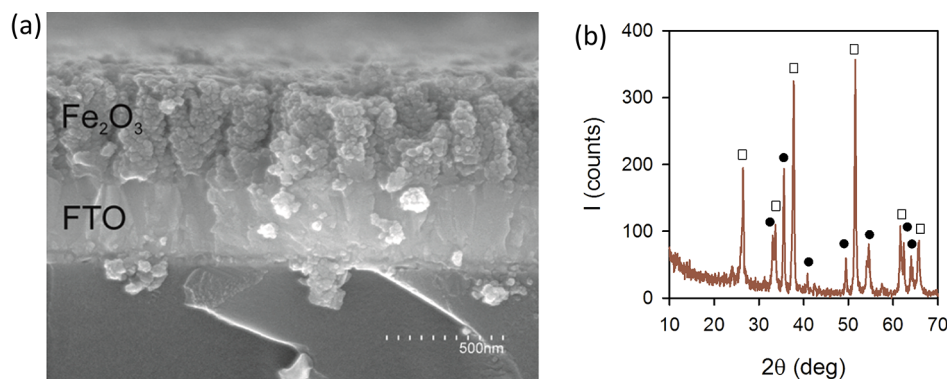

Figure 1. (a) SEM micrograph of a cross section of FTO/Fe$_2$O$_3$. (b) XRD spectrum of a FTO/Fe$_2$O$_3$ sample. All the diffraction peaks were identified corresponding to FTO (□) and Fe$_2$O$_3$ (●) phases.

through the substrate. Consequently, there was no competition between Fe_2O_3 and the iridium layer to absorb visible light.

RESULTS AND DISCUSSION

Figure 1a shows a cross section of a representative FTO/Fe_2O_3 film. The thickness of the Fe_2O_3 layer is around 300 nm, and its morphology appears as the cauliflower-like structures previously reported by Gratzel and co-workers.[17,41] XRD has confirmed the monophase nature of the material, α-Fe_2O_3, as illustrated in Figure 1b.

The optical properties of the material are shown in Figure 2. The optical bandgap could be estimated by the Tauc plot for
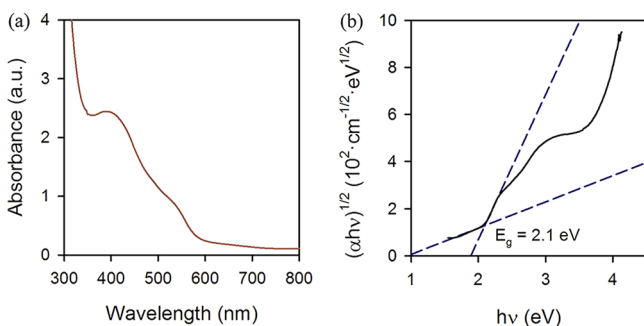

Figure 2. (a) Optical density of a FTO/Fe_2O_3 representative sample. (b) Tauc plot for an indirect bandgap semiconductor, $r = 1/2$, indicating a value $E_g = 2.1$ eV for hematite.

indirect bandgap transitions[42] ($r = 1/2$) (Figure 2b). The obtained value was $E_g = 2.1$ eV in excellent agreement with the reported values for hematite, $E_g = 2.1$–2.2 eV.[43]

After the electrodeposition of the iridium complex, a clear darker layer appears on top of the reddish hematite, which was previously identified as the blue layer (BL).[32] Surface analyses of selected Fe_2O_3 samples with electrodeposited iridium oxides obtained from 10 μM, 1 mM, and 5 mM [Cp*Ir] solutions were carried out by XPS. An example of the obtained spectra is shown in the Supporting Information, Figure SI1. The surface concentration of Ir was estimated as 0.48 atom %, 3.9 atom %, and 5.7 atom %, respectively. The carbon content in the electrodeposited iridium material may be originated from carboxylic acid oxidation product functioning as an O-donor to iridium.[39] Additionally, carbonate species may originate from the oxidative degradation of the Cp* ligand.[32] A significant contribution of the O signal can be ascribed to the Ir–O bonding, and after spectra deconvolution, the obtained stoichiometry for the deposited IrO_x phase is $x = 2.1$, $x = 2.2$, and $x = 2.1$ for 10 μM, 1 mM, and 5 mM solutions, respectively. Moreover, the analysis of the Fe signal confirmed the stoichiometry of the Fe_2O_3 phase in all cases.

The photoelectrochemical properties of the Fe_2O_3 specimens before and after electrodeposition of different amounts of iridium were tested by cyclic voltammetry. Although the electrodeposited IrO_x layer absorbs visible light (see Supporting Information, Figure SI2), since samples were illuminated through the substrate, there was no competition between Fe_2O_3 and the IrO_x layer to absorb visible light. Figure 3 shows the results obtained in the dark and under illumination. Upon deposition of the iridium material from low concentrated solutions (5 and 10 μM), two distinct features can be observed in the dark j–V curves (Figure 3a). First, the catalytic wave for water oxidation at 1.7 V vs RHE is enhanced by the addition of iridium. Second, the capacitive feature centered at 0.8 V vs RHE
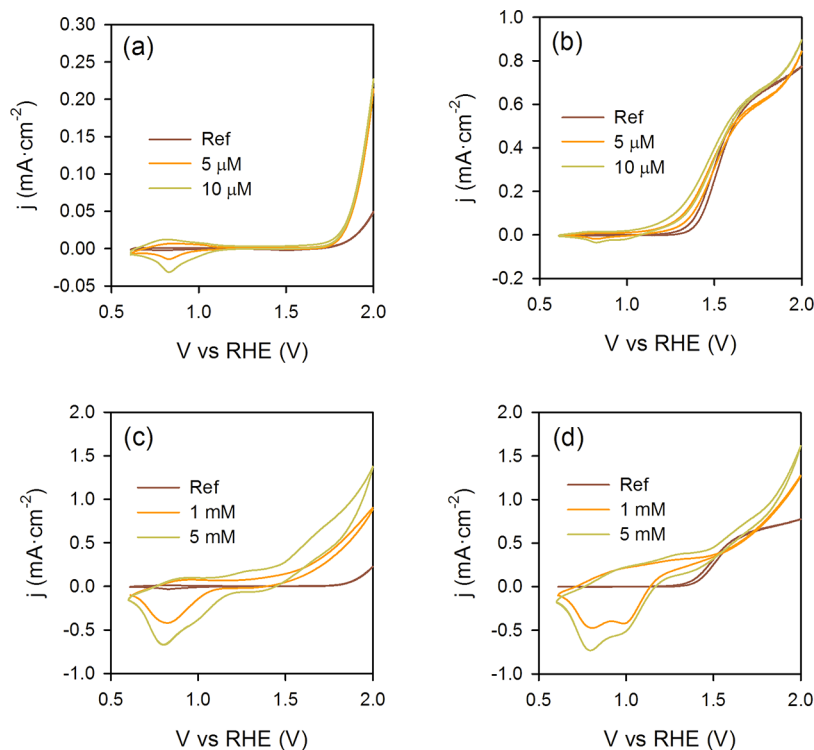

Figure 3. Cyclic voltammetry curves obtained in the dark and under illumination at 100 mW·cm^{-2} for a reference Fe_2O_3 sample (ref) and after electrodeposition of [Cp*Ir] from solutions with different concentrations. The scan rate was 10 mV·s^{-1}. (a) 5 and 10 μM in the dark, (b) 5 and 10 μM under illumination, (c) 1 and 5 mM in the dark, and (d) 1 and 5 mM under illumination.
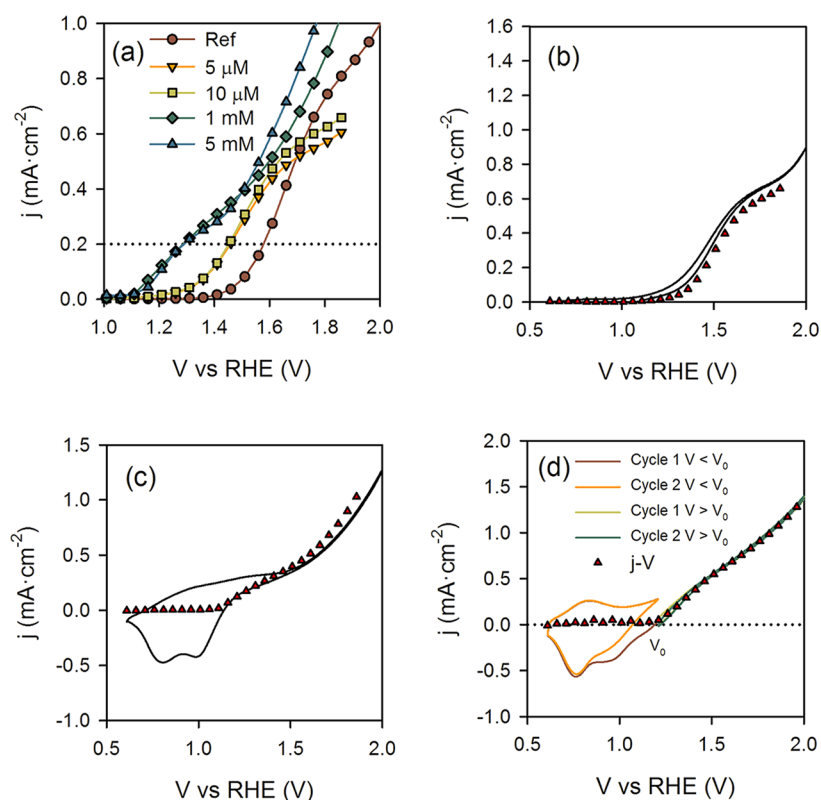
Figure 4. (a) Steady-state $j-V$ curves for bare Fe_2O_3 (ref) and after electrodeposition of $[Cp*Ir]$ from solutions with different concentrations (5 μM, 10 μM, 1 mM, and 5 mM). The lines are included as eyeguides. Comparison between cyclic voltammetry (lines) and steady-state (red dots) $j-V$ curves for Fe_2O_3 samples after electrodeposition of $[Cp*Ir]$ from solutions with different $[Cp*Ir]$ concentrations of (b) 10 μM and (c) 1 mM. (d) Cyclic voltammetry curves with the starting potential at the photocurrent onset (V_0) and steady-state $j-V$ curves for the Fe_2O_3/IrO_x sample after electrodeposition of $[Cp*Ir]$ from 1 mM solution.

is in good agreement with previous studies with iridium oxide films. This reversible wave has been ascribed to a Ir(III)/Ir(IV) redox process, which involves a two-electron, three-proton process.[32,44] Under illumination (Figure 3b), a cathodic shift of the onset potential for water oxidation takes place upon Ir addition, which increases with the electrodeposited Ir content. At high $[Cp*Ir]$ concentrations (1 and 5 mM), both in the dark (Figure 3c) and under illumination (Figure 3d), the electrode behavior is dominated by the large capacitance stemming from the Ir(III)/Ir(IV) redox process,[45,46] and water oxidation clearly takes place at more cathodic potentials as the Ir content increases in the film.

A clearer picture of the photoelectrochemical behavior of the tested samples is provided by the steady-state $j-V$ curves. For these measurements, the photocurrent was sampled after stabilizing over several minutes for individual potentials, and the obtained results are shown in Figure 4a. Direct comparison of the steady-state $j-V$ curve and cyclic voltammetry curves of Figure 3 are presented as Figure 4b and Figure 4c for Fe_2O_3 samples after electrodeposition of $[Cp*Ir]$ from 10 μM and 1 mM solutions, respectively. For the other concentrations, results are shown as Supporting Information, Figure SI3. In all cases, the obtained agreement is very good. The higher values of photocurrent obtained for some of the steady-state $j-V$ curves at high anodic bias indicate some diffusion limitations, which have been highlighted elsewhere.[47] On the other hand, from these steady-state $j-V$ curves, the beneficial effect of $[Cp*Ir]$ cathodically shifting the potential for water oxidation is even more evident compared to cyclic voltammetry curves since the effect of capacitance is absent. As a reference, the potentials

needed to sustain a photocurrent of 200 μA·cm^{-2} (dotted line in Figure 4a) are compiled in Table 1 together with the cathodic

Table 1. Potential Required to Sustain a Photocurrent of 200 μA·cm^{-2} from the Steady-State $j-V$ Curves in Figure 4 for Bare Hematite (Ref) and after Electrodeposition of $[Cp*Ir]$ from Solutions with Different Concentrations (5 μM, 10 μM, 1 mM, and 5 mM)^a

sample	$V@j = 200$ μA·cm^{-2} (V vs RHE)	ΔV (mV)
ref	1.58	0
5 μM	1.46	129
10 μM	1.45	130
1 mM	1.29	300
5 mM	1.29	300

^{a}The cathodic shift (ΔV) with respect to bare hematite is also indicated.

shifts with respect to bare hematite (ΔV). These values are in reasonably good correspondence with those derived from Figure 3. Moreover, the cathodic shifts obtained in the present study are in excellent agreement with those reported by Tilley et al. after electrophoretic deposition of IrO_2 nanoparticles.[17] In that study, a 200 mV cathodic shift was reported for a surface concentration of 1 atom % iridium, while 130 mV is obtained in the present study for 0.5 atom % iridium. At high concentrations of Ir (electrodeposition from 1 and 5 mM solutions), a remarkable 300 mV cathodic shift is obtained.

Further evidence to assign the steady-state photocurrent to water oxidation was carried out by running cyclic voltammetry

curves with the initial potential at the onset potential for the photocurrent (V_0). This representation allows a clear deconvolution of the IrO_x capacitive processes ($V < V_0$) and the faradaic water oxidation process ($V > V_0$). An example is shown in Figure 4d for Fe_2O_3/IrO_x (from 1 mM solution). The first two scans at $V > V_0$ and $V < V_0$ are represented together with the steady-state $j-V$ curve, clearly indicating that $V > V_0$ corresponds to water oxidation. Additionally, to rule out other possible processes (i.e., IrO_x oxidation), 20 consecutive cyclic voltammetry scans were carried out under illumination for samples with different surface concentrations of iridium. The results are shown as Supporting Information, Figure SI4. At low Ir concentration (deposition from 10 μM [Cp*Ir] solution), the repeatability of the scans clearly indicated that the IrO_x layer was stable and did not oxidize during testing. At high Ir concentrations (deposition from 1 mM [Cp*Ir] solution), there was a systematic shift of the cyclic voltammetry curves with the number of cycles. This suggests that progressive oxidation of the iridium-based layer took place during photoelectrochemical testing. However, this effect is clearly separated from the steady-state photocurrent for water oxidation reported in Figure 4.

Further insight into the water oxidizing mechanisms was provided by electrochemical impedance spectroscopy (EIS). To analyze the physicochemical processes responsible for the traffic of carriers within the material and at the interface with the aqueous solution, a physical model is required. We already developed a physical model, which accounted for the relevant processes leading to water oxidation for Fe_2O_3 synthesized by atomic layer deposition (Supporting Information, Figure SI5).[10,11,16] The equivalent circuit (EC) consists of the capacitance of the bulk hematite, C_{bulk}, charge transfer resistance from the valence band of the hematite, $R_{ct,bulk}$, a resistance which is related to the rate of trapping holes in surface states, R_{trap}, a capacitance of the surface states, C_{trap}, and charge transfer resistance from the surface states, $R_{ct,trap}$.[11] We showed that the photocurrent onset was coincident with the charging of a surface state and the decrease of the charge transfer resistance from this surface state, $R_{ct,trap}$. This behavior clearly indicated that hole transfer predominantly takes place by a surface state. In the present study, identical behavior was observed (Figure 5), and consequently, an analogous water oxidation mechanism can be safely proposed for APCVD hematite.

Experimentally, we did not observe the presence of any additional arc in the obtained Nyquist plots after the deposition of the IrO_x layer compared to bare Fe_2O_3. However, to account for the presence of this IrO_x layer, we will now consider the
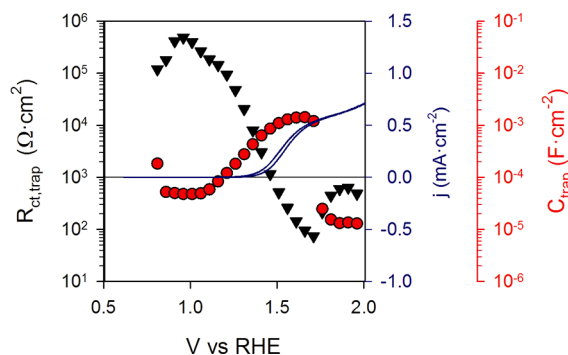
model scheduled by the EC shown in Figure 6. This EC is similar to that developed for bare hematite and includes some extra
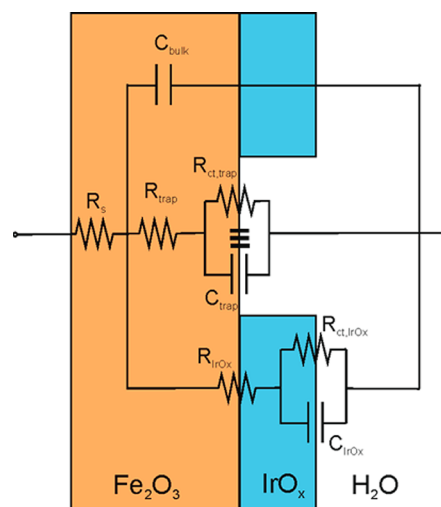

Figure 6. Equivalent circuit employed for the interpretation of hematite electrodes coated with an IrO_x catalyst.

elements to account for the IrO_x layer: the capacitance of the IrO_x layer, C_{IrOx}, and charge transfer resistance from the IrO_x layer, $R_{ct,IrOx}$. To unambiguously fit the experimental impedance spectra obtained, we have defined the capacitance of the Fe_2O_3/IrO_x layer, as $C_{film} = C_{bulk} + C_{trap} + C_{IrOx}$, and the charge transfer resistance from the film, R_{ct}, as the parallel combination of $R_{ct,trap}$ and $R_{ct, IrOx}$. Consequently, the analyzed circuit is similar to that scheduled in the Supporting Information, Figure SI5d.

Some examples of the Nyquist plots experimentally obtained together with the fittings to the employed physical models for the tested samples are compiled as Supporting Information, Figure SI6. The quality of the fitting to the experimental spectra was systematically good for all the tested samples, with fitting errors below 5% for all the extracted parameters. The results obtained from fitting the experimental impedance to the model scheduled in Figure 6 are shown in Figure 7.

It is clear that C_{film} is dominated by the capacitance of the IrO_x layer (C_{IrOx}) at low potentials (0.5−1.2 V vs RHE) since this capacitance is increasing with the thickness of the IrO_x layer (Figure 7a and Figure 7c). The peaks at 0.8−0.9 V vs RHE are consistent with the reversible wave observed by cyclic voltammetry shown in Figure 3, corresponding to the Ir(III)/Ir(IV) redox process. This capacitance is also responsible for the hysteresis observed in the cyclic voltammetry curves (Figure 3), particularly at high surface concentrations of Ir.

After the deposition of low amounts of the Ir complex onto hematite (from 5 and 10 μM solutions), the same correlation shown in Figure 5 is obtained between the photocurrent onset, C_{film} and R_{ct} (Supporting Information, Figure SI2). The lower R_{ct} values (Figure 7b) satisfactorily explain the cathodic shift of the photocurrent for water oxidation observed in Figure 3 and Figure 4. At higher Ir concentrations (from 1 and 5 mM solutions), the capacitance of the IrO_x layer becomes very large and clearly dominates the capacitance of the electrode. A close look at Figure 7b and Figure 7d indicates that the charge transfer resistance decreases upon increasing the iridium concentration on the Fe_2O_3 surface, reflecting that Fe_2O_3 photogenerated holes may be efficiently transferred to the IrO_x layer, where water oxidation takes place. Facile kinetics of hole transfer from the IrO_x layer for
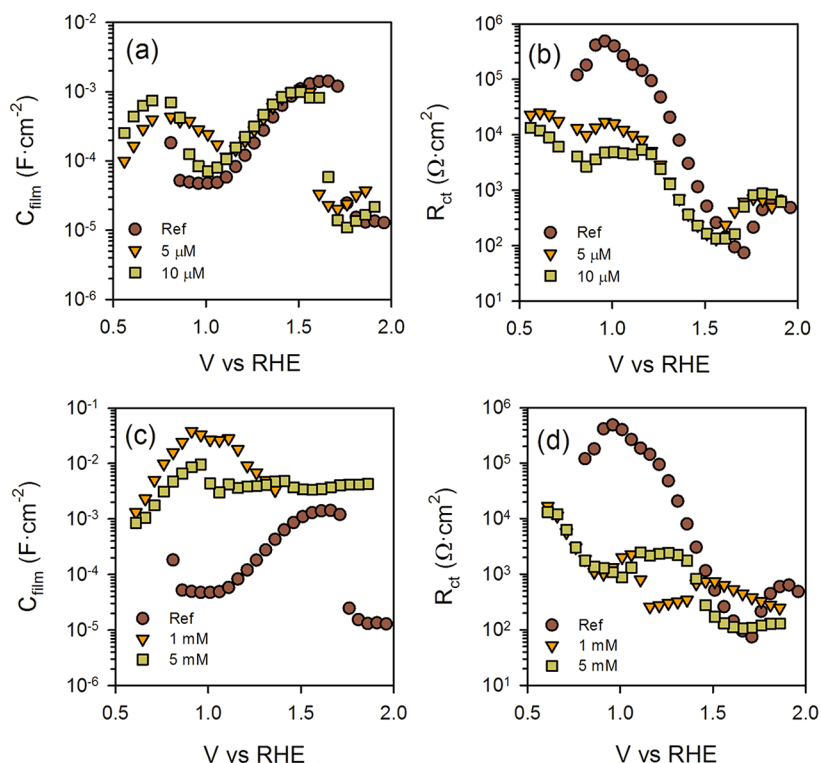

Figure 5. Photocurrent (j), charge transfer resistance from a surface state ($R_{ct,trap}$), and trap capacitance (C_{trap}) for a reference hematite sample.

Figure 7. Capacitance, C_{film} (a and c), and charge transfer resistance, R_{ct} (b and d), for the Fe_2O_3/IrO_x films from low concentrated solutions (a and b) and high concentrated solutions (c and d).

the oxygen evolution reaction may also contribute to the lowered charge transfer resistance. This supports the idea that the process follows a similar mechanism as that recently proposed for the effect of the Co–Pi catalyst.[16] The low values of R_{ct} are responsible for the photocurrents of 0.2 $mA \cdot cm^{-2}$ for water oxidation at potentials as low as 1.3 V vs RHE (Figure 4).

Moreover, it is relevant to determine whether the cathodic shift produced upon Ir electrodeposition is related to a shift of the conduction band due to the presence of a dielectric layer. Consequently, we analyzed the behavior of the bulk capacitance of Fe_2O_3 (C_{bulk}) in the dark, as shown in the Mott–Schottky plot of Figure 8. For the different concentrations of Ir employed, the donor density (N_D) and flat band potential (V_{FB}) were compared (Table 2). From the comparison of the data, it can be inferred that the V_{FB} value does not depend on the concentration of
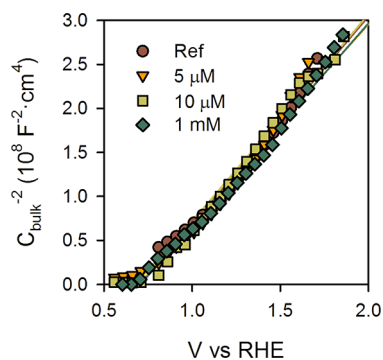
Table 2. Flat Band Potential (V_{FB}) and Donor Density (N_D) for Fe_2O_3 before (Ref) and after Electrodeposition of [Cp*Ir] from Solutions with Different Concentrations (5 μM, 10 μM, 1 mM, and 5 mM)

sample	V_{FB} (V vs RHE)	N_D ($\times 10^{22}$ cm^{-3})
ref	0.71	1.87
5 μM	0.67	1.98
10 μM	0.70	1.87
1 mM	0.70	1.92

iridium, therefore indicating that the cathodic shift is not due to a conduction band shift. A similar behavior was observed upon deposition of the Co–Pi catalyst on Fe_2O_3.[16] Additionally, these values of flat band potential are in good agreement with previously reported values for hematite synthesized by different processes.[10,11,16] The high values of N_D ($\sim 10^{22}$ cm^{-3}) for these films are in reasonably good agreement with the values reported for APCVD hematite ($10^{20}–10^{21}$ cm^{-3}).[48,49]

All these experiments support the idea that the catalytic effect of the IrO_x layer can be interpreted in terms of a highly capacitive layer. This layer stores the photogenerated holes at Fe_2O_3 by oxidation of Ir(III) to Ir(IV). Consequently, the transfer of photogenerated holes to the IrO_x layer significantly reduces recombination with conduction band electrons, which is responsible for the beneficial cathodic shift observed for water oxidation.

CONCLUSIONS

In this work, we synthesized APCVD Fe_2O_3 films, and we evaluated the effect of an electrodeposited [Cp*Ir] catalyst on the photoelectrochemical water oxidation performance. Structural and surface analysis of the electrodeposited films showed that the Ir layer preferentially possesses stoichiometry IrO_x, with

Figure 8. Mott–Schottky plot of the bulk capacitance of hematite, after deposition of a IrO_x layer from solutions with different concentrations of the [Cp*Ir] catalyst (5 μM, 10 μM, and 1 mM). The results for bare hematite are also included as a reference.

$x \approx 2.1$ for the Ir-containing layers obtained from solutions with different concentrations of the [IrCp*] source. The cathodic potential shift for the water photo-oxidation increased upon increasing the amount of the electrodeposited Ir catalyst. Remarkably, a 300 mV shift at 200 μA·cm^{-2} photocurrent was obtained for the highest surface concentrations of IrO$_x$ tested. We have interpreted the catalytic mechanism of the iridium-containing film on the basis of a highly capacitive layer, which enhances charge separation and can store photogenerated holes at Fe$_2$O$_3$, subsequently oxidizing water, with lower surface recombination compared to bare Fe$_2$O$_3$. These findings constitute an important step forward in the understanding of the mechanism operating in the water oxidation by heterogeneous Ir-based catalysts coupled with semiconductor materials.

■ ASSOCIATED CONTENT

Ⓢ Supporting Information

XPS spectra, absorbance spectra of Fe$_2$O$_3$/IrO$_x$ films, comparison between cyclic voltammetry and steady-state j–V curves for samples containing different concentrations of the iridium complex, consecutive cyclic voltammetry scans for Fe$_2$O$_3$/IrO$_x$ samples to rule out IrO$_x$ oxidation, physical model for water splitting with Fe$_2$O$_3$, examples of impedance spectra and fitting to the physical model, and relationship between photocurrent, charge transfer resistance, and capacitance. This material is available free of charge via the Internet at http://pubs.acs.org.

■ AUTHOR INFORMATION

Corresponding Author
*(S.G.) +34964387554, sjulia@uji.es; (E.P.) +34964387518, eperis@uji.es; (J.B.) +34964387541, bisquert@uji.es.

Notes
The authors declare no competing financial interest.

■ ACKNOWLEDGMENTS

■ REFERENCES

(1) Barber, J. Photosynthetic Energy Conversion: Natural and Artificial. *Chem. Soc. Rev.* **2009**, *38*, 185−196.

(2) Chen, X. B.; Shen, S. H.; Guo, L. J.; Mao, S. S. Semiconductor-Based Photocatalytic Hydrogen Generation. *Chem. Rev.* **2010**, *110*, 6503−6570.

(3) van de Krol, R.; Liang, Y. Q.; Schoonman, J. Solar Hydrogen Production with Nanostructured Metal Oxides. *J. Mater. Chem.* **2008**, *18*, 2311−2320.

(4) Walter, M. G.; Warren, E. L.; McKone, J. R.; Boettcher, S. W.; Mi, Q. X.; Santori, E. A.; Lewis, N. S. Solar Water Splitting Cells. *Chem. Rev.* **2010**, *110*, 6446−6473.

(5) Hamann, T. W. Splitting Water with Rust: Hematite Photoelectrochemistry. *Dalton Trans.* **2012**, *41*, 7830−7834.

(6) Sivula, K.; Le Formal, F.; Gratzel, M. Solar Water Splitting: Progress Using Hematite (Alpha-Fe2O3) Photoelectrodes. *ChemSusChem.* **2011**, *4*, 432−449.

(7) Lin, Y. J.; Yuan, G. B.; Sheehan, S.; Zhou, S.; Wang, D. W. Hematite-Based Solar Water Splitting: Challenges and Opportunities. *Energy Environ. Sci.* **2011**, *4*, 4862−4869.

(8) Lin, Y. J.; Zhou, S.; Sheehan, S. W.; Wang, D. W. Nanonet-Based Hematite Heteronanostructures for Efficient Solar Water Splitting. *J. Am. Chem. Soc.* **2011**, *133*, 2398−2401.

(9) Alexander, B. D.; Kulesza, P. J.; Rutkowska, L.; Solarska, R.; Augustynski, J. Metal Oxide Photoanodes for Solar Hydrogen Production. *J. Mater. Chem.* **2008**, *18*, 2298−2303.

(10) Klahr, B.; Gimenez, S.; Fabregat-Santiago, F.; Bisquert, J.; Hamann, T. W. Electrochemical and Photoelectrochemical Investigation of Water Oxidation with Hematite Electrodes. *Energy Environ. Sci.* **2012**, *5*, 7626−7636.

(11) Klahr, B.; Gimenez, S.; Fabregat-Santiago, F.; Hamann, T.; Bisquert, J. Water Oxidation at Hematite Photoelectrodes: The Role of Surface States. *J. Am. Chem. Soc.* **2012**, *134*, 4294−4302.

(12) Hisatomi, T.; Le Formal, F.; Cornuz, M.; Brillet, J.; Tetreault, N.; Sivula, K.; Graetzel, M. Cathodic Shift in Onset Potential of Solar Oxygen Evolution on Hematite by 13-Group Oxide Overlayers. *Energy Environ. Sci.* **2012**, *4*, 2512−2515.

(13) Lin, Y. J.; Xu, Y.; Mayer, M. T.; Simpson, Z. I.; McMahon, G.; Zhou, S.; Wang, D. W. Growth of p-Type Hematite by Atomic Layer Deposition and Its Utilization for Improved Solar Water Splitting. *J. Am. Chem. Soc.* **2012**, *134*, 5508−5511.

(14) Kanan, M. W.; Nocera, D. G. In Situ Formation of an Oxygen-Evolving Catalyst in Neutral Water Containing Phosphate and Co2+. *Science* **2008**, *321*, 1072−1075.

(15) Zhong, D. K.; Cornuz, M.; Sivula, K.; Graetzel, M.; Gamelin, D. R. Photo-Assisted Electrodeposition of Cobalt-Phosphate (Co-Pi) Catalyst on Hematite Photoanodes for Solar Water Oxidation. *Energy Environ. Sci.* **2012**, *4*, 1759−1764.

(16) Klahr, B.; Gimenez, S.; Fabregat-Santiago, F.; Bisquert, J.; Hamann, T. W. Photoelectrochemical and Impedance Spectroscopic Investigation of Water Oxidation with "Co-Pi" Coated Hematite Electrodes. *J. Am. Chem. Soc.* **2012**, *134*, 16693−16700.

(17) Tilley, S. D.; Cornuz, M.; Sivula, K.; Gratzel, M. Light-Induced Water Splitting with Hematite: Improved Nanostructure and Iridium Oxide Catalysis. *Angew. Chem., Int. Ed.* **2010**, *49*, 6405−6408.

(18) Trasatti, S. Electrocatalysis by Oxides - Attempt at a Unifying Approach. *J. Electroanal. Chem.* **1980**, *111*, 125−131.

(19) Mills, A.; Russell, T. Comparative Study of New and Established Heterogeneous Oxygen Catalysts. *J. Chem. Soc., Faraday Trans.* **1991**, *87*, 1245−1250.

(20) Zhao, Y. X.; Hernandez-Pagan, E. A.; Vargas-Barbosa, N. M.; Dysart, J. L.; Mallouk, T. E. A High Yield Synthesis of Ligand-Free Iridium Oxide Nanoparticles with High Electrocatalytic Activity. *J. Phys. Chem. Let.* **2011**, *2*, 402−406.

(21) Zhao, Y. X.; Vargas-Barbosa, N. M.; Hernandez-Pagan, E. A.; Mallouk, T. E. Anodic Deposition of Colloidal Iridium Oxide Thin Films from Hexahydroxyiridate(IV) Solutions. *Small* **2011**, *7*, 2087−2093.

(22) Nakagawa, T.; Beasley, C. A.; Murray, R. W. Efficient Electro-Oxidation of Water near Its Reversible Potential by a Mesoporous IrO$_x$ Nanoparticle Film. *J. Phys. Chem. C* **2009**, *113*, 12958−12961.

(23) Profeti, D.; Lassali, T. A. F.; Olivi, P. Preparation of Ir0.3Sn(0.7-x)TixO2 Electrodes by the Polymeric Precursor Method: Characterization and Lifetime Study. *J. Appl. Electrochem.* **2006**, *36*, 883−888.

(24) Sardar, K.; Fisher, J.; Thompsett, D.; Lees, M. R.; Clarkson, G. J.; Sloan, J.; Kashtiban, R. J.; Walton, R. I. Structural Variety in Iridate Oxides and Hydroxides from Hydrothermal Synthesis. *Chem. Sci.* **2011**, *2*, 1573−1578.

(25) Mugavero, S. J.; Smith, M. D.; Yoon, W. S.; zur Loye, H. C. Nd2K2IrO7 and Sm2K2IrO7: Iridium(VI) Oxides Prepared Under Ambient Pressure. *Angew. Chem., Int. Ed.* **2009**, *48*, 215−218.

(26) Trasatti, S. Electrocatalysis in the Anodic Evolution of Oxygen and Chlorine. *Electrochim. Acta* **1984**, *29*, 1503−1512.

(27) Stonehar. P.; Kozlowsk, Ha; Conway, B. E. Potentiodynamic Examination of Electrode Kinetics for Electroactive Adsorbed Species -

Applications to Reduction of Noble Metal Surface Oxides. *Proc. R. Soc. London, Ser. A* **1969**, *310*, 541.

(28) Rand, D. A. J.; Woods, R. Cyclic Votammetryc Studies of Iridium Electrodes in Sulfuric Acid Solutions - Nature of Oxygen Layer and Metal Dissolution. *J. Electroanal. Chem.* **1974**, *55*, 375−381.

(29) Capon, A.; Parsons, R. Effect of Strong Acid on Reactions of Hydrogen and Oxygen Noble-Metals - Study Using Cyclic Voltammetry and a New Teflon Electrode Holder. *J. Electroanal. Chem.* **1972**, *39*, 275.

(30) Buckley, D. N.; Burke, L. D. Oxygen Electrode. 5. Enhancement of Charge Capacity of an Iridium Surface in Anodic Region. *J. Chem. Soc., Faraday Trans. I* **1975**, *71*, 1447−1459.

(31) Pickup, P. G.; Birss, V. I. A Model for Anodic Hydrous Oxide - Growth at Iridium. *J. Electroanal. Chem.* **1987**, *220*, 83−100.

(32) Blakemore, J. D.; Schley, N. D.; Olack, G. W.; Incarvito, C. D.; Brudvig, G. W.; Crabtree, R. H. Anodic Deposition of a Robust Iridium-Based Water-Oxidation Catalyst from Organometallic Precursors. *Chem. Sci.* **2011**, *2*, 94−98.

(33) Hull, J. F.; Balcells, D.; Blakemore, J. D.; Incarvito, C. D.; Eisenstein, O.; Brudvig, G. W.; Crabtree, R. H. Highly Active and Robust Cp* Iridium Complexes for Catalytic Water Oxidation. *J. Am. Chem. Soc.* **2009**, *131*, 8730 +..

(34) Hetterscheid, D. G. H.; Reek, J. N. H. Me-2-NHC Based Robust Ir Catalyst for Efficient Water Oxidation. *Chem. Commun. (Cambridge, U. K.)* **2010**, *47*, 2712−2714.

(35) McDaniel, N. D.; Coughlin, F. J.; Tinker, L. L.; Bernhard, S. Cyclometalated Iridium(III) Aquo Complexes: Efficient and Tunable Catalysts for the Homogeneous Oxidation of Water. *J. Am. Chem. Soc.* **2008**, *130*, 210−217.

(36) Blakemore, J. D.; Schley, N. D.; Balcells, D.; Hull, J. F.; Olack, G. W.; Incarvito, C. D.; Eisenstein, O.; Brudvig, G. W.; Crabtree, R. H. Half-Sandwich Iridium Complexes for Homogeneous Water-Oxidation Catalysis. *J. Am. Chem. Soc.* **2010**, *132*, 16017−16029.

(37) Parent, A. R.; Brewster, T. P.; De Wolf, W.; Crabtree, R. H.; Brudvig, G. W. Sodium Periodate as a Primary Oxidant for Water-Oxidation Catalysts. *Inorg. Chem.* **2012**, *51*, 6147−6152.

(38) Hintermair, U.; Hashmi, S. M.; Elimelech, M.; Crabtree, R. H. Particle Formation during Oxidation Catalysis with Cp* Iridium Complexes. *J. Am. Chem. Soc.* **2012**, *134*, 9785−9795.

(39) Blakemore, J. D.; Schley, N. D.; Kushner-Lenhoff, M. N.; Winter, A. M.; D'Souza, F.; Crabtree, R. H.; Brudvig, G. W. Comparison of Amorphous Iridium Water-Oxidation Electrocatalysts Prepared from Soluble Precursors. *Inorg. Chem.* **2012**, *51*, 7749−7763.

(40) Schley, N. D.; Blakemore, J. D.; Subbaiyan, N. K.; Incarvito, C. D.; D'Souza, F.; Crabtree, R. H.; Brudvig, G. W. Distinguishing Homogeneous from Heterogeneous Catalysis in Electrode-Driven-Water Oxidation with Molecular Iridium Complexes. *J. Am. Chem. Soc.* **2011**, *133*, 10473−10481.

(41) Kay, A.; Cesar, I.; Graetzel, M. New Benchmark for Water Photooxidation by Nanostructured α-Fe$_2$O$_3$ Films. *J. Am. Chem. Soc.* **2006**, *128*, 15714−15721.

(42) Chen, Z. B.; Jaramillo, T. F.; Deutsch, T. G.; Kleiman-Shwarsctein, A.; Forman, A. J.; Gaillard, N.; Garland, R.; Takanabe, K.; Heske, C.; Sunkara, M.; et al. Accelerating Materials Development for Photoelectrochemical Hydrogen Production: Standards for Methods, Definitions, and Reporting Protocols. *J. Mater. Res.* **2010**, *25*, 3−16.

(43) Hardee, K. L.; Bard, A. J. Semiconductor Electrodes. Application of Chemically Vapor-Deposited Iron-Oxide Films to Photosensitized Electrolysis. *J. Electrochem. Soc.* **1976**, *123*, 1024−1026.

(44) Burke, L. D.; Whelan, D. P. A New Interpretation of the Charge Storage and Electrical-Conductivity Behavior of Hydrous Iridium Oxide. *J. Electroanal. Chem.* **1981**, *124*, 333−337.

(45) Hu, C. C.; Huang, Y. H.; Chang, K. H. Annealing Effects on the Physicochemical Characteristics of Hydrous Ruthenium and Ruthenium-Iridium Oxides for Electrochemical Supercapacitors. *J. Power Sources.* **2002**, *108*, 117−127.

(46) Lokhande, C. D.; Dubal, D. P.; Joo, O.-S. Metal Oxide Thin Film Based Supercapacitors. *Curr. Appl. Phys.* **2011**, *11*, 255−270.

(47) Shimizu, K.; Lasia, A.; Boily, J. F. Electrochemical Impedance Study of the Hematite/Water Interface. *Langmuir* **2012**, *28*, 7914−7920.

(48) Cesar, I.; Sivula, K.; Kay, A.; Zboril, R.; Graetzel, M. Influence of Feature Size, Film Thickness, and Silicon Doping on the Performance of Nanostructured Hematite Photoanodes for Solar Water Splitting. *J. Phys. Chem. C* **2009**, *113*, 772−782.

(49) Le Formal, F.; Tetreault, N.; Cornuz, M.; Moehl, T.; Gratzel, M.; Sivula, K. Passivating Surface States on Water Splitting Hematite Photoanodes with Alumina Overlayers. *Chem. Sci.* **2011**, *2*, 737−743.